Optical design and performance testing of an athermal SWIR gas correlation imager

A. Tanbakuchi*[a], M. Smith [a], J. Mercier [a], S. Vigil [a], T. Embree [a], A. Ison [a]

[a]Sandia National Laboratories, P.O. Box 5800, Albuquerque, NM 87184-0406

ABSTRACT

Gas correlation imagers are important instruments for remotely detecting effluent emissions. However, making a functional design for field testing is non-trivial given the range of environmental conditions the system may be operated under and the required matched imaging performance for both channels. We present a dual channel 7 degree full field of view f/2.5 athermal optical design athermalized from 0 to 50 degrees C that operates in the wavelength range of 2.0 to 2.5 microns suitable for methane imaging. We present the optical design, tolerance budget, and alignment plan used for the system. Predicted and as-built performance data including interferometric and ensquared energy measurements for both imaging channels are also shown.

Keywords: gas correlation imager, athermal optical design, SWIR imager

1. INTRODUCTION

Gas correlation radiometry is a proven[1,2,3,4,5,6,7,8] highly sensitive technique for remotely detecting gas emissions. The method works by taking the difference of two measurements to detect the presence of a specific gas. The first measurement passes light though a cell containing the gas that is to be detected. The second measurement passes the light through a reference cell that does not contain the gas of interest. The reference cell can either be evacuated or filled with an optically inert gas. Gas molecules typically have unique molecular resonances that appear as extremely narrow lines that are grouped into absorption bands. By using a band pass filter to isolate measurements to a unique resonance band and combining this with a gas cell that correlates to all of the absorption lines of a specific molecule within that band it becomes possible to detect the presence of a specific gas with high sensitivity and specificity. In the presence of the gas of interest, both measurements will have decreased transmission. In the absence of the gas of interest, only the channel with the gas present in the cell will observe strong absorption. Therefore, the gas can be detected when the difference between the two channels is reduced. Furthermore, calibration of the system enables not only detection of the gas, but also inferences on the column of gas in the scene.

Gas correlation radiometry can be realized in either active or passive form. Our interest is building a passive detection system for methane gas. Because methane gas has a strong resonance band centered around 2.258 um and the reflected solar radiance in this band is appreciable, it is possible to build a passive SWIR gas correlation imager using a InSb detector array that can operate at video rates. However, making a gas correlation imager that can operate in diverse field conditions while providing matched imaging between channels is a non-trival task. In this paper, we discuss the development of the optical system for a first generation field prototype gas correlation imager designed to detect methane gas. In the following sections we discuss the basic optical requirements, the optical design process, tolerancing of the system, and the as-built optical performance.

2. SYSTEM DESIGN

To enable methane gas imaging as well as support calibrations for water vapor and other spurious signals, a design was developed that enables collection across the 2.0-2.5 um short wave infrared (SWIR) band. To provide sufficient scene resolution and sensitivity the system requires a 96 mm focal length f/2.5 lens combined with a 30 um pitch 320 x 256 pixel detector. The complete optical system design parameters and as-built image performance goals are shown in Table 1.

*email: atanbak@sandia.gov, phone: (505) 284-4306

The overall optical layout is shown in Figure 1. The system has a common aperture where the light passes through a narrow-band filter centered on the strong methane absorption band. Then the signal is split into two optical paths by a 50/50 beam splitter. Both paths are identical; they contain a gas cell, an athermal lens, and a dewar containing a cold stop, short pass filter and an InSb detector. The gas cell in one path contains methane while the gas cell in the other path is filled with an optically inert gas to serve as a reference channel. Other than having different contents in the gas cells, the paths are designed to be identical. The athermal optics enables operation across a wide range of temperatures (0 to 50 degrees C) without the need to refocus.

Table 1. Key optical system parameters and design goals.

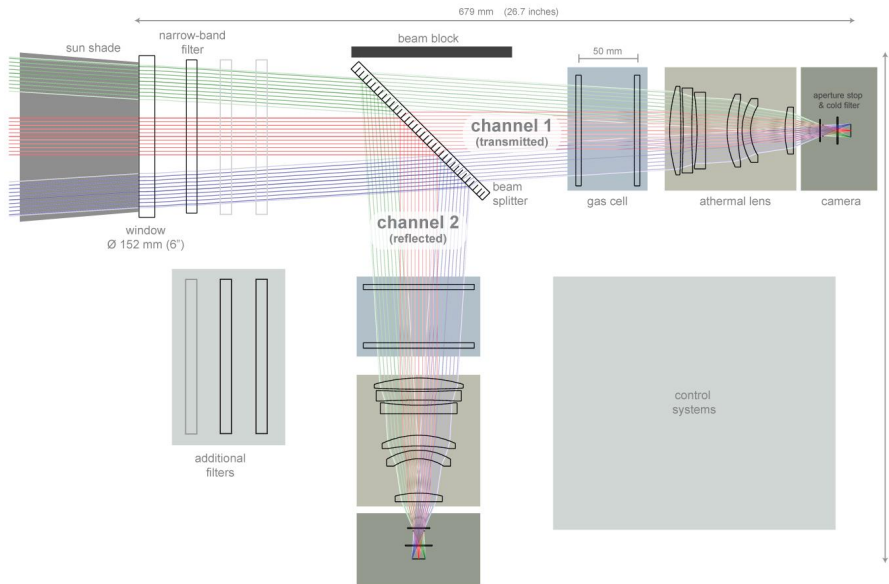| Parameter	Value
Spectral band	2.0-2.5 um
athermal temperature range	0 - 50 deg C
F-number	f/2.5
focal length	96 mm
entrance pupil dia	28.4 mm
full field of view	4.7 x 5.7 deg
detector pixel pitch	30 um
detector pixels	320 x 256
MTF goal at 16.6 cycle/mm	at least 50% for optics
30 um ensquared energy goal	70% or greater
depth of field	0.2 km to infinity

Figure 1. Gas correlation imager system layout.

During the initial optical design process, it was determined that an athermal optical design was needed to ensure the focus was maintained across the operational temperature range. To minimize the need for active optical components (such as focus controls), a passive athermal system was designed. To illustrate the need for chromatic and athermal correction, a simple silicon objective was first designed. Figure 2 shows an all silicon objective that is comparable in size to the final athermal objective. The left group of spots in Figure 3 demonstrates that the all silicon objective is limited by chromatic aberration and thermal defocus.
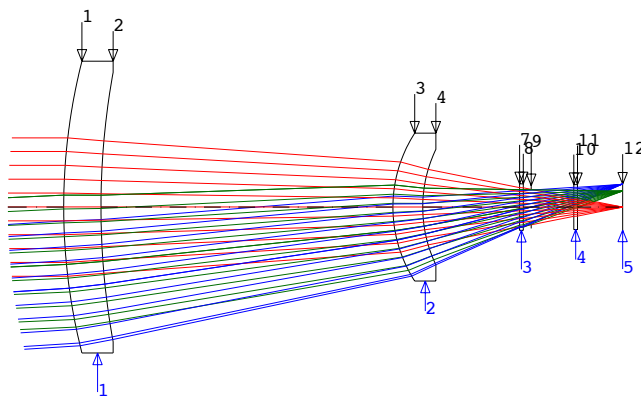

Figure 2. Simple all silicon objective that satisfies system aperture and FOV requirements. Both powered elements are spherical silicon lenses. Surface 9 is the cold stop. The two plane parallel plates are the dewar window and the short pass filter.

To achieve an athermal optical design that operates from 2–2.5 um, a minimum of three optical materials are required. Two materials are needed to provide the chromatic correction. A third material is needed to maintain the focus across the desired temperature range. We followed the approach described by Tamagawa[9] to determine the initial athermal achromat starting point. First, the chromatic dispersive power versus the thermal dispersive power for the five candidate optical materials with acceptable optical and mechanical properties in the spectral range of 2–2.5 um were plotted (Figure 5). If three materials are chosen such that they maximize the enclosed triangular area, the optical design will be 'relaxed' requiring the minimum amount of bending at each optical surface. This minimizes the higher order aberrations generated in the optical design and leads to looser optical and mechanical tolerances. The chart illustrates that two relaxed options exist, silicon, zinc sulphide, and calcium fluoride, or barium fluoride, zinc sulphide, and calcium fluride. Of these two options, the first one is more favorable because silicon has a higher index of refraction and barium fluoride is more fragile and not as readily available. Given the three chosen materials — silicon, zinc sulphide multi-spectral (Cleartran), and calcium fluoride — and the CTE of the mechanical housings (aluminum), an initial starting solution can be analytically determined for the athermal design.

Due to the moderate f-number, field of view, and rear cold stop design constraints of the system, a single all spherical athermal triplet does not have sufficient capability to provide good aberration correction across the field of view with reasonable tolerances. Therefore, the starting design was composed of two athermal triplets with the power split between them. With the initial analytical design work complete, the starting perscription proved to be excellent. Only minor optimization was done to better balance the aberrations across the field. It was also possible to substitute ZnS for the second CaF2 element. Minimizing the use of CaF2 is favorable due to the more complex mechanical mounts required to hold this fragile material. The final athermal and achromatic objective design is shown in Figure 4. The improvement in the chromatic and athermal performance is shown compared to the all silicon objective in Figure 3. The new objective design maintains nearly all the energy within a 30 um pixel (reference square) across the wavelength and temperature ranges of interest. Furthermore, the overlaid circles representing the airy disk diameter indicate that the system is approximately diffraction limited. Figure 6 illustrates the athermal correction by plotting the field average RMS spot diameter as a function of temperature for the athermal objective and all silicon objective.

Figure 7 shows the MTF performance across the field for the athermal lens. The nominal MTF at the detector Nyquist frequency (16.6 cycles/mm) is greater than 80% across the field. Figure 8 plots the ensquared energy across the 0–50 degree C operational temperature range. The ensquared energy represents the percent of energy that falls within one pixel. The ensquared energy is extremely stable, staying within 85–90%. Compared to the as-built design goals of MTF

and ensqured energy shown in Table 1, the nominal system design exceeds the goals. In the following section covering tolerancing, it will be shown that the margin from the residual enables reasonable fabrication tolerances.
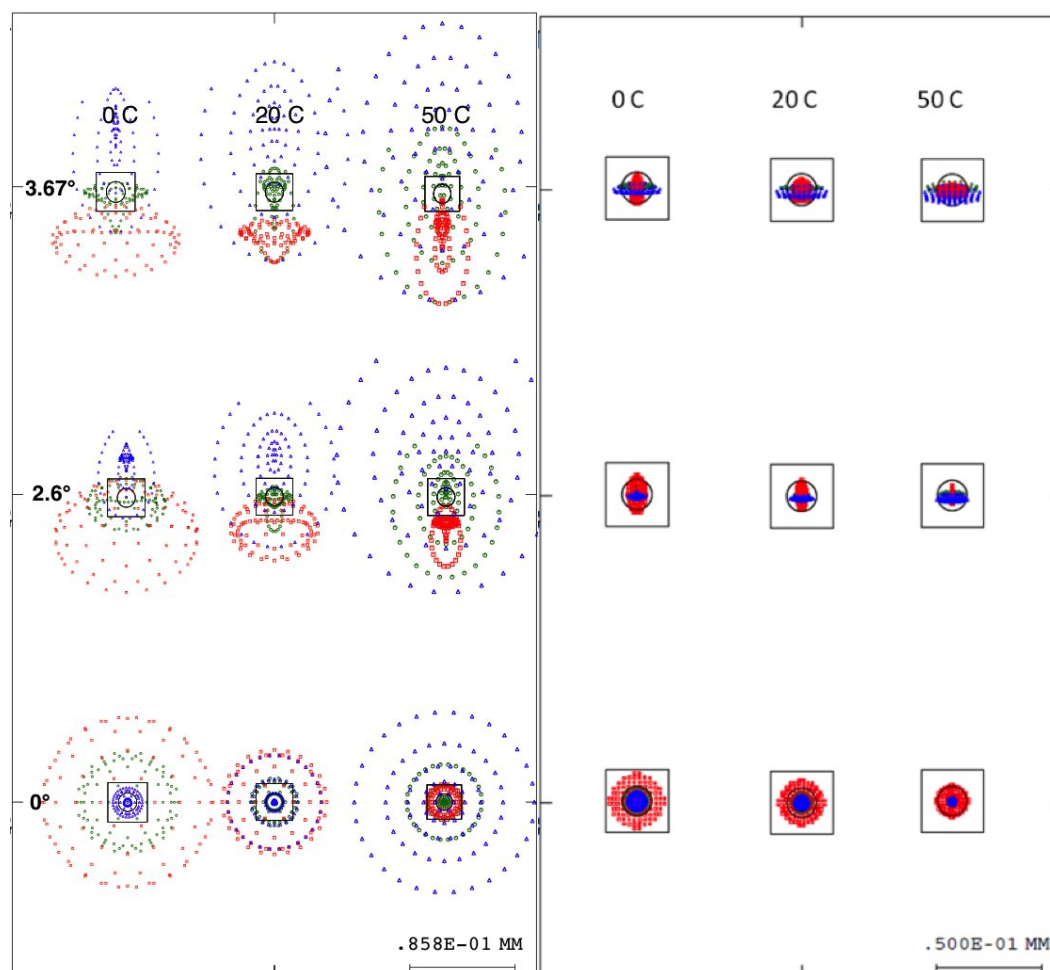

Figure 3. Spot diagrams for Si objective (left set) and athermal lens (right set). For each group the columns represent different temperatures and the rows represent different field angles. The squares show the size of a 30 um pixel and the circles represent the airy disk. The Si objective spots illustrate that the lens is dominated by chromatic aberration as well as having moderate focus change with temperature.
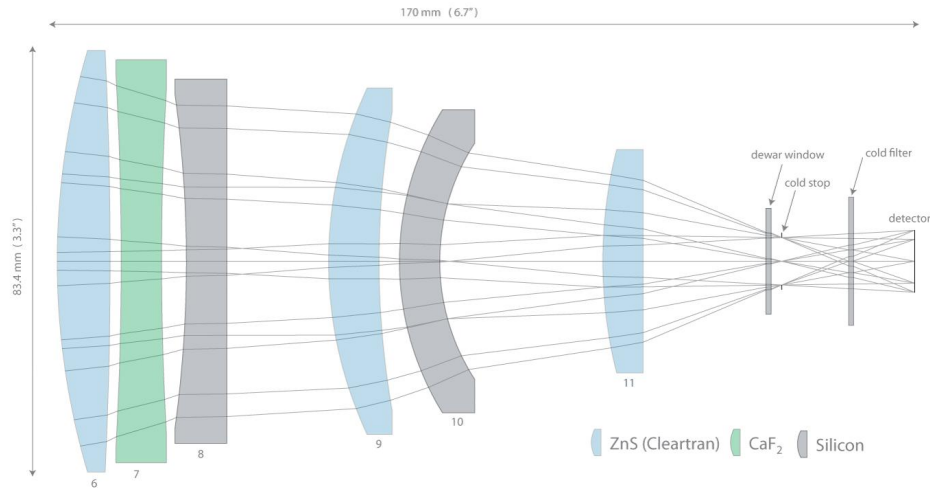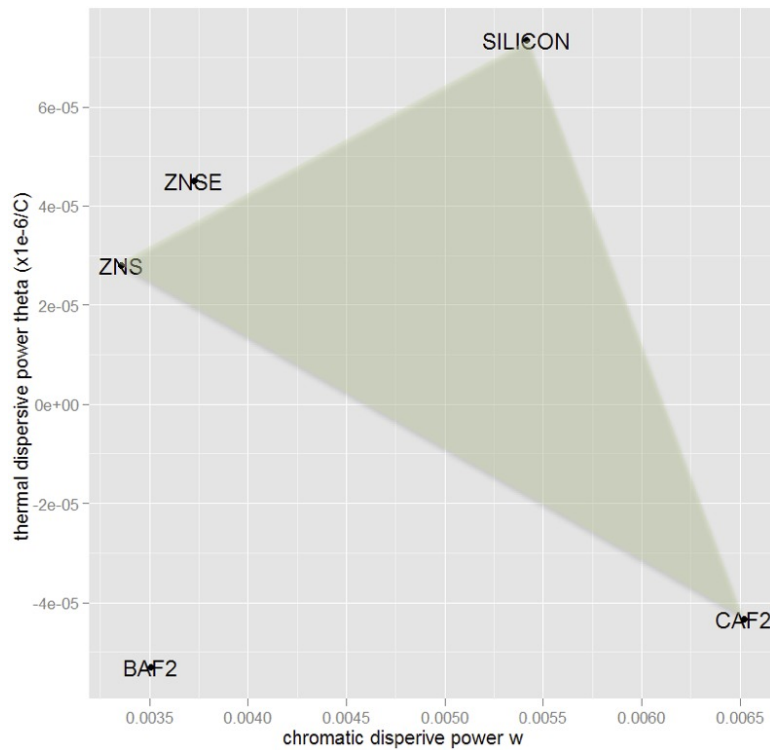
Figure 4. Athermal objective.

Figure 5. Athermal chart for the candidate optical materials. Maximizing the area enclosed by three materials minimizes the amount of bending in the triplet yielding a relaxed design. Because of the less favorable properties of BaF2, the best combination is ZnS, CaF2, and Silicon.
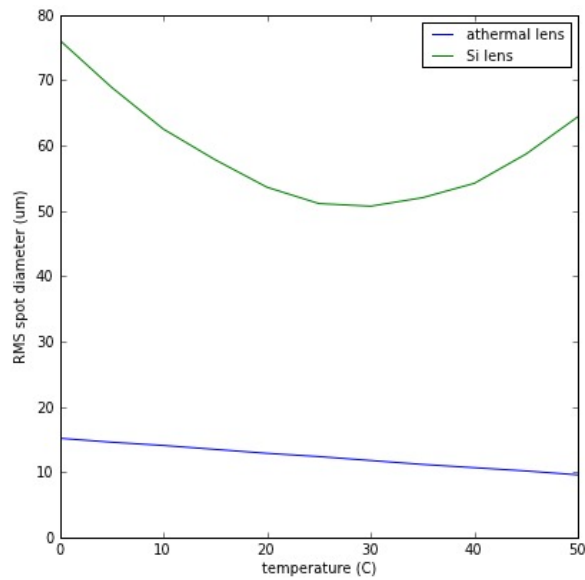
Figure 6. Comparison of RMS spot diameter versus temperature for the athermal lens and reference Si lens. The athermal lens is much more stable across the full temperature range. The residual thermal performance variation is insignificant compared to the 30 um pixel size.
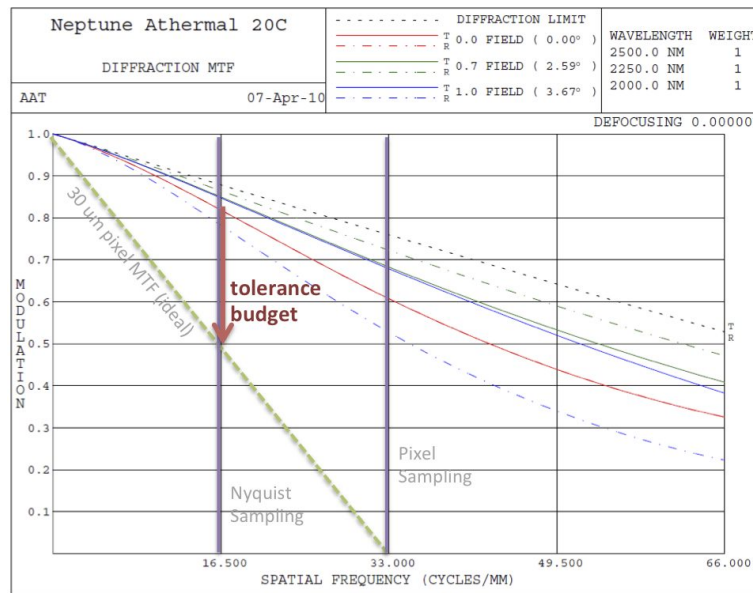

Figure 7. Nominal MTF of the optical system. With the as-built goal of a 50% optical MTF, sufficient margin exists for reasonable fabrication and alignment tolerances.
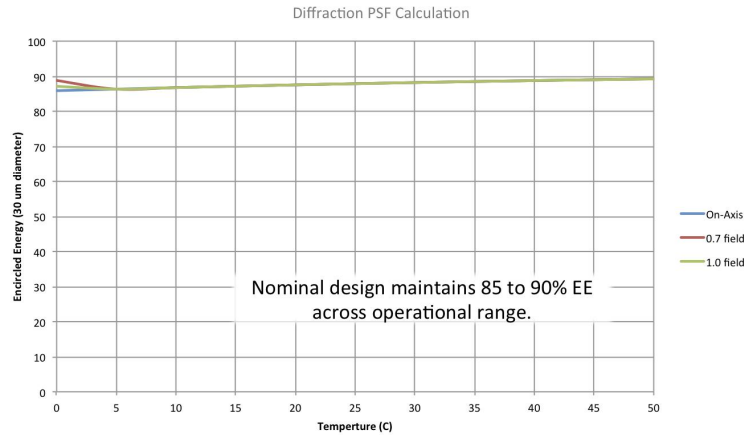
Figure 8. Athermal performance shown in terms of encircled energy for a 30 um diameter pixel. In terms of this performance metric which integrates the detector pitch, the system performance is predicted to be extremely stable.

3. TOLERANCING

The as-built design goal for the optical system is an MTF of at least 50% at the detector Nyquist sampling frequency or an ensqured energy of at least 70%. Since the detector pixel pitch is 30 um, the Nyquist frequency is 16.6 cycles per mm. Ideally, the MTF of the detector at this frequency is limited to 50%, therefore if the as-built optics provide an MTF of at least 50% we can maintain approximately 25% modulation of the combined optics and detector system.

Due to the relaxed nature of the optical design, it was possible to utilize relatively loose tolerances. The element tolerances enable cost effective standard lens fabrication techniques to be used. The alignment tolerances enabled simple lens cell mounting and alignment with existing tooling. The range of tolerances used for the fabrication and alignment are summarized in Table 2 and Table 3. The only compensator used was tilt and focus of the detector, which was easily accommodated with the dewar chamber mount.

Table 2: Fabrication tolerances for the optical components.

Parameter	Tolerance
Thickness	2 - 8 mils
wedge	0.5 - 4.5 arc min
irregularity	0.5 - 3 waves
power	2 - 12 waves

Table 3: Alignment tolerances for the opto-mechanical components.

Parameter	Tolerance
despace	4 - 16 mils
tilt	1 - 10 arc min
decenter	6 - 8 mils

Using our optical model with the detailed tolerances, it is possible to statistically estimate the as-built MTF. Figure 11 plots the cumulative probability density function for the MTF. It indicates that at the 97.7% probability level, the optical system will achieve an MTF of 50% or better across the field of view at the detector Nyquist frequency. In fact, other than the edge of the field of view, the as-built MTF values should substantially exceed this target. The plot indicates that there still is some design margin to allow us to meet our as-built goals if a few components fall slightly outside their tolerance bounds. The optical model also predicts an ensquared energy of 77.5% on average on and off-axis when accounting for a finite laboratory source size, finite source test distance, and the assigned tolerances.
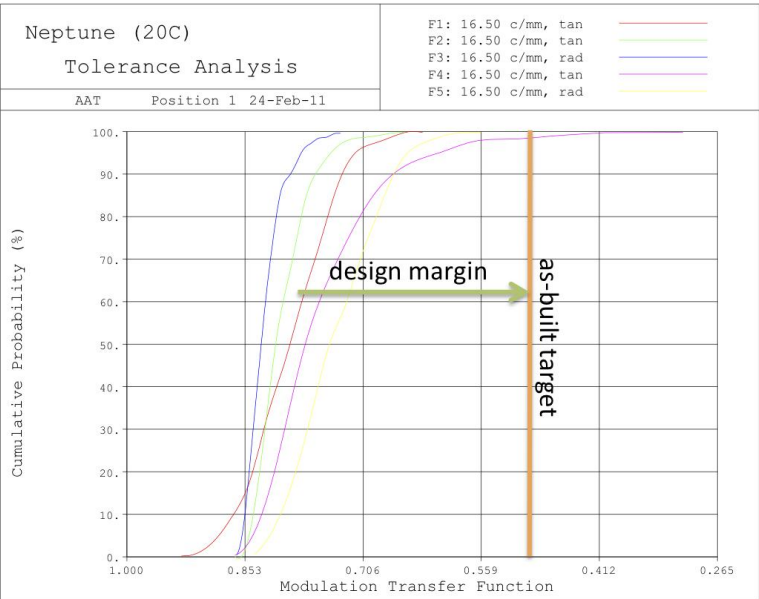

Figure 9. Statistical tolerance analysis of MTF.

4. ALIGNMENT

For the alignment of the optical system, both mechanical and optical techniques were used. To reduce the stack up of mechanical tolerances in the athermal objective, the front group of 3 elements and rear group of 3 elements were mounted in separate sub-cells (details of the opto-mechanical design are detailed in a separate publication[10]). Then the two sub-cells were aligned together. For the powered optics sub-cells, the loose tolerances allowed the optics to be aligned by their mechanical seats in the housings. Figure 10 illustrates the opto-mechanical assembly for the athermal objective and shows the actual objective during alignment. To align the two sub-cells to one another, a theodolite was used. First the rear half of the sub cell was aligned onto the theodolite optical axis using the front and rear reflected pips from the ZnS lens as well as the front reflected pip from the silicon lens. Next, the axial despace between the two sub-cells was set using gauge blocks (shown in Figure 10). Then using the adjustable rods that hold the two cells together, the front half was aligned to the theodolite axis using the front and rear pips from the ZnS and CaF2 elements.
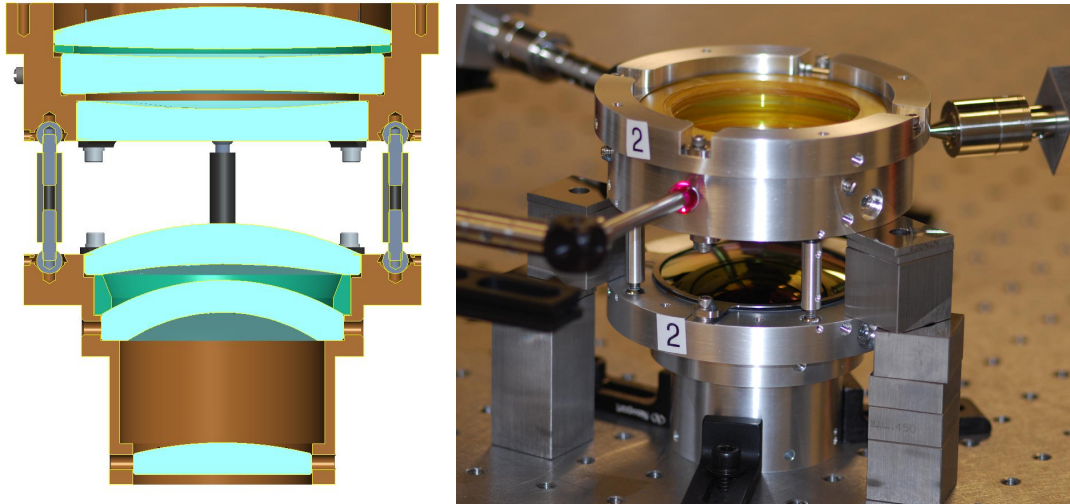
Figure 10. Schematic of the opto-mechanical assembly of athermal objective (left) and image of both halves of the athermal objective being optically aligned (right) to a theodolite axis (above out of picture).

Figure 11 shows how the complete optical train was aligned. Because there are two paths in the system that are split with a SWIR 50/50 beam splitter, the only custom alignment tool required was a beam alignment plate. To align the system, a theodolite was set up in front of the entrance aperture of the system such that the front most pip was no closer than the minimum focus of the theodolite.

To align the path that is reflected by the beam splitter, a 45 degree prism was placed with its hypotenuse coincident with the front beam splitter surface plane. At this point the theodolite was looking down to the detector in the reflected channel. Next the InSb detector in the dewar chamber (without cold filter) was aligned. The back reflection from the detector was used to align the detector tip and tilt. To center the detector, the theodolite was focused on the detector surface and rotated to measure the offset of the edges. Once the offsets were symmetrical, the detector was centered on the theodolite axis. Next, the powered optics were aligned using the pips from the front two elements.
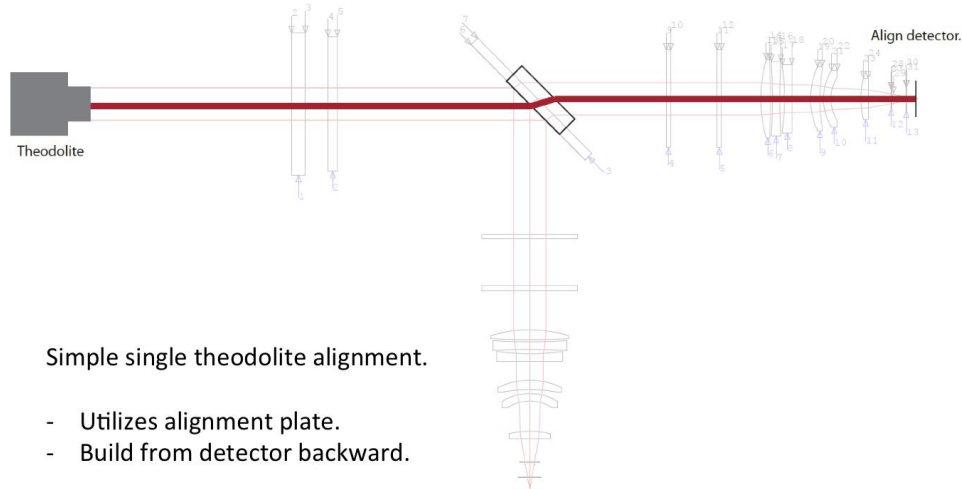

Figure 11. Technique for aligning the optical system with a theodolite.

To align the transmitted path, the beam alignment plate was placed at 45 degrees to the theodolite such that the front surface was coincident with the location that the beam splitter would later be installed. The alignment plate, made from BK7, was tolerance to ensure that it would deviate the theodolite line of sight the same amount as the final silicon beam splitter. Once the alignment plate was installed, the procedure to align the transmitted path detector and athermal objective is the same as the reflected path.

The gas cells, beam splitter, narrowband filters, and window were the final components to be aligned. The gas cells were easily aligned using their back reflections into the theodolite. Centering was again done by checking the edge offset angles. Figure 12 shows the SWIR beam splitter being aligned using the pips from the reflected path athermal lens. Finally, the narrow band filters and window were placed and aligned with their back reflections.
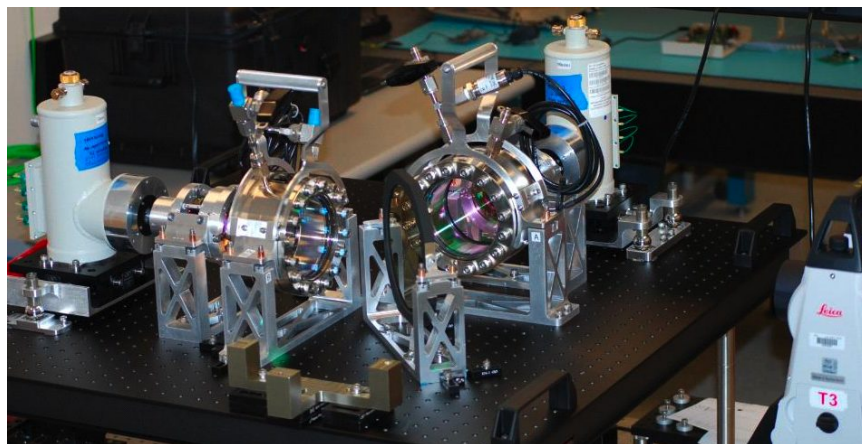

Figure 12. Optical setup during alignment of the SWIR beam splitter.

5. AS-BUILT PERFORMANCE

Before integrating the athermal objectives into the full system, the as-built performance was measured interferometrically. Each powered lens set was placed in front of a 1550 nm interferometer and tested in double pass configuration with a reflecting reference sphere centered at the image point. Measurements were taken both on and off-axis by rotating the lens.
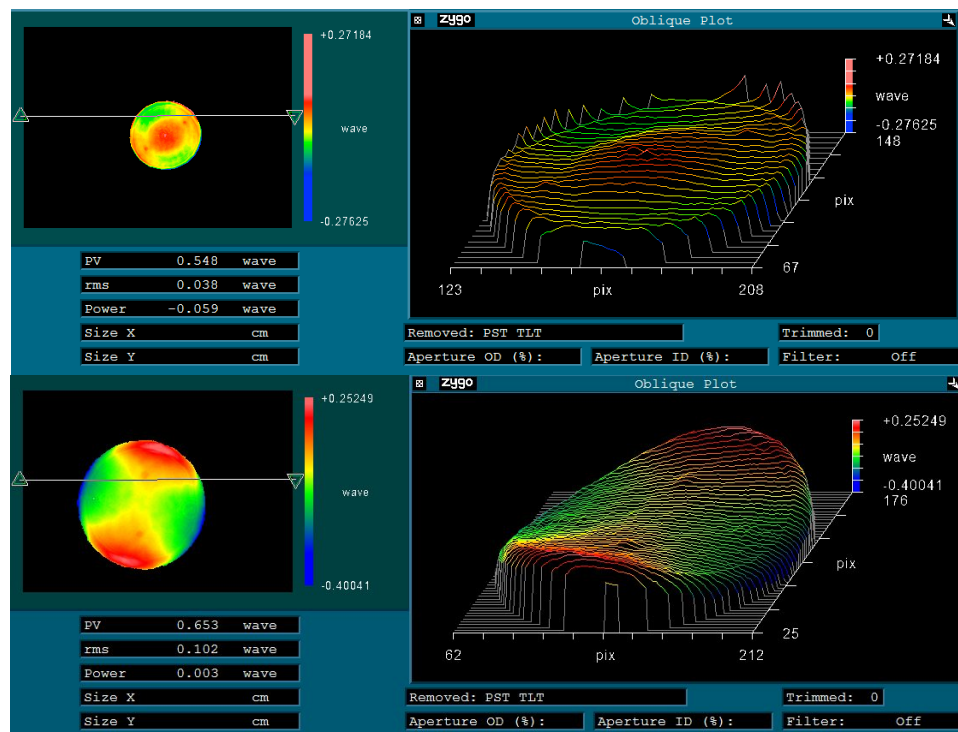

Figure 13. Athermal objective 1 on-axis (top) and off-axis (bottom) measured wavefront error.
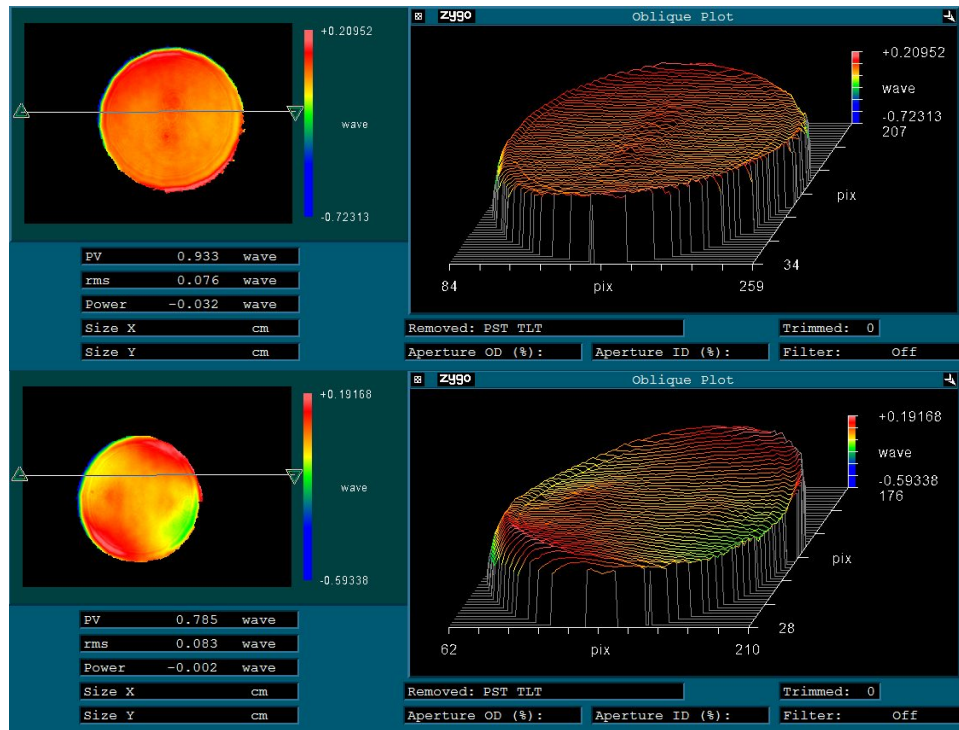
Figure 14. Athermal objective 2 on-axis (top) and off-axis (bottom) measured wavefront error.

The wavefront measurements are shown in Figure 13 and Figure 14 for the two objectives. Table 4 summarizes the measured data against the optical model. An optical system is considered diffraction limited if the RMS wavefront error is 1/14 wave or less at the operating wavelength. Since the optics were measured at 1550 nm, they would need on RMS of no more than 0.104 waves at 1550 nm to be diffraction limited at 2.25 um. The results show that the as-built system is diffraction limited on and off-axis. Off axis, the performance is slightly worse as expected. The as-built values all come in less than those predicted at the 97.7% level, as expected from the results shown in Figure 9.

Table 4. Powered optics interferometric as-built measurements at 1550 nm. Optical model values are also reported at the 97.5% level for 1550 nm. As-built values in parenthesis indicate the percentile performance.

Setup	RMS WFE 0 deg	RMS WFE 2.6 deg
OPTICAL MODEL		
Design Residual	0.014	0.043
Modelled Tolerances	(97.7%) 0.112	(97.7%) 0.234
MEASURED		
Cell 1	(70%) 0.079	(55%) 0.103
Cell 2	(70%) 0.075	(40%) 0.083

To provide a full system test once the athermal lenses were integrated into the complete optical setup, ensquared energy measurements were made. To collect this data, the setup consisted of a black body point source located roughly 10 m away from the input aperture of the optical system. It projected a point source that was less than 1/4 of a pixel. By rotating the optical system about the entrance pupil, the on and off axis performance could be measured.

The collected point source images used to compute ensquared energy are shown in Figure 15. The measurements made with a black body at a finite distance have excellent agreement with the optical model. The optical model predicts an ensquared energy of 77.5% on average for on and off-axis when accounting for the finite source size, finite source distance, and the tolerances. The measured ensquared energy values ranged from 70% to 82% for the two channels on and off-axis. Preliminary ensquared energy measurements across a limited temperature range have shown that the variation with temperature appears to follow the model results shown in Figure 8.
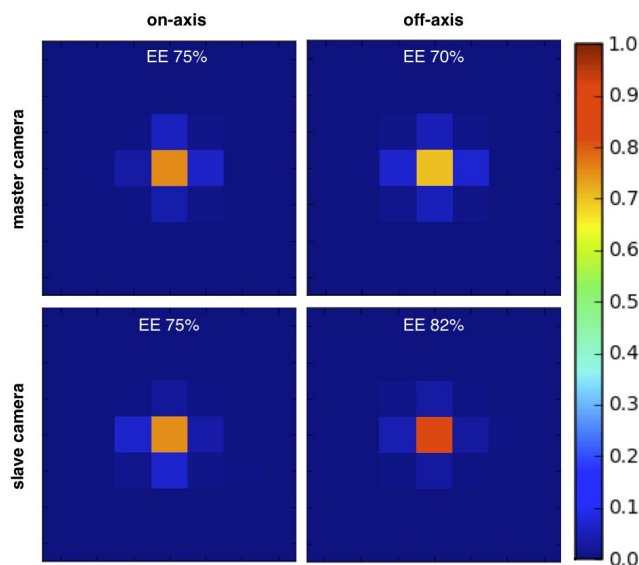

Figure 15. System ensquared energy measurements. Data represents a 7 x 7 pixel ROI showing a point source black body (1/4 pixel in physical extend) imaged through the optics onto the detector. The optical model predicts an ensquared energy of 77.5% on average on and off-axis when accounting for the finite source size, finite source distance, and the tolerances.

6. CONCLUSIONS

In this paper we have described the design technique used to successfully develop an athermal and achromatic SWIR matched dual channel gas correlation imaging system. By utilizing an analytical technique to develop a relaxed and well-corrected starting design, it was possible to create a moderately loosely tolerance optical design. The reasonable tolerance enabled cost effective component fabrication and a simple alignment technique. The result was a successful system build with as-built data meeting our design requirements and matching our initial optical model predictions.

7. FUTURE WORK

The next phase of this work involves a number of tasks. We plan to (1) characterize the athermal performance across the full range of operational temperatures, (2) fully calibrate the system, (3) develop real time algorithms for processing the real-time video data and presenting quantitative gas measurements, and (4) conduct field tests with the complete instrument to demonstrate it's sensitivity and specificity to methane gas detection.

Acknowledgements

REFERENCES

[1] Sandsten, J., Weibring, P., Edner, H., and Svanberg, S., "Real-time gas-correlation imaging employing thermal background radiation," Optics Express 6(4), 92–103 (2000).

[2] III, J.M.R., Gordley, L.L., Park, J.H., Drayson, S.R., Hesketh, W.D., Cicerone, R.J., Tuck, A.F., Frederick, J.E., Harries, J.E., et al., "THE HALOGEN OCCULTATION EXPERIMENT," Journal of Geophysical Research 98(D6), PP. 10,777–10,797.

[3] Patra, P.K., Lal, S., Chand, D., and others, "Halogen Occultation Experiment (HALOE) and balloon-borne in situ measurements of methane in stratosphere and their relation to the quasi-biennial oscillation (QBO)," Atmospheric Chemistry and Physics Discussions 3(2), 1925–1947 (2003).

[4] Drummond, J.R., and Mand, G.S., "The Measurements of Pollution in the Troposphere (MOPITT) Instrument: Overall Performance and Calibration Requirements," Journal of Atmospheric and Oceanic Technology 13(2), 314–320 (1996).

[5] Gordley, L.L., McHugh, M.J., Marshall, B.T., and Thompson, E., "Digital array gas radiometer (DAGR): a sensitive and reliable trace gas detection concept," Proceedings of SPIE 7312(1), 73120F–73120F–7 (2009).

[6] Gordley, L.L., Hervig, M.E., Fish, C., and McHugh, M.J., "Trace gas detection and monitoring with the Digital Array Gas-correlation Radiometer (DAGR)," Proceedings of SPIE 8024(1), 80240U–80240U–8 (2011).

[7] Larsen, N.F., and Stamnes, K., "Methane detection from space: use of sunglint," Optical Engineering 45(1), 016202–016202–8 (2006).

[8] Gordley, L.L., and Marshall, B.T., "Doppler wind and temperature sounder: new approach using gas filter radiometry," Journal of Applied Remote Sensing 5(1), 053570–053570–21 (2011).

[9] Tamagawa, Y., Wakabayashi, S., Tajime, T., and Hashimoto, T., "Multilens system design with an athermal chart," Applied Optics 33(34), 8009–8013 (1994).

[10] Ison, A.M., Sanchez, R.M., Kumpunen, M.A., Dilworth, S.G., Martin, J.W., Chaplya, P.M., and Franklin, J.W., "Optomechanical design for cost-effective DEMVAL systems," Proceedings of SPIE 8125(1), 812502–812502–12 (2011).